Short lifetimes of organic nitrates in a sub-urban temperate forest indicate efficient assimilation of reactive nitrogen by the biosphere

Simone T. Andersen[1], Rolf Sander[1], Patrick Dewald[1], Laura Wüst[1], Tobias Seubert[1], Gunther N. T. E. Türk[1], Jan Schuladen[1], Max R. McGillen[2], Chaoyang Xue[2], Abdelwahid Mellouki[2,3], Alexandre Kukui[4], Vincent Michoud[5], Manuela Cirtog[5], Mathieu Cazaunau[5], Astrid Bauville[5], Hichem Bouzidi[5], Paola Formenti[5], Cyrielle Denjean[6], Jean-Claude Etienne[6], Olivier Garrouste[6], Christopher Cantrell[7], Jos Lelieveld[1], John N. Crowley[1]

[1]Atmospheric Chemistry Department, Max-Planck-Institute for Chemistry, 55128-Mainz, Germany

[2]Institut de Combustion, Aérothermique, Réactivité Environnement (ICARE), CNRS, 1C Avenue de la Recherche Scientifique, CEDEX 2, 45071 Orléans, France

[3]University Mohammed VI Polytechnic (UM6P), Lot 660, Hay Moulay Rachid Ben Guerir, 43150, Morocco

[4]Laboratoire de Physique et Chimie de l'Environnement et de l'Espace (LPC2E), CNRS Orléans, France

[5]Université Paris Cité and Univ Paris Est Creteil, CNRS, LISA, F-75013 Paris, France

[6]CNRM, Universite de Toulouse, Meteo-France, CNRS, Toulouse, France

[7]Univ Paris Est Creteil and Université de Paris Cité, CNRS, LISA, F-94010 Créteil, France

Correspondence to: Simone T. Andersen (simone.andersen@mpic.de) and John N. Crowley (john.crowley@mpic.de)

1   Abstract

Alkyl nitrates (ANs) and peroxycarboxylic nitric anhydrides (PANs) are important reservoirs
of reactive nitrogen that contribute significantly to the rate of formation and growth of
secondary organic aerosols and support the transport of reactive nitrogen from polluted areas
to remote areas. It is therefore critical to understand their sources and sinks in different
environments. In this study we use measurements of OH, O_3, NO_3 reactivity, VOCs, $\sum$ANs
and $\sum$PANs during the ACROSS campaign to investigate different production and loss
processes of ANs and PANs in a temperate forest. At daytime OH-initiated processes were the
dominant source of ANs (69-72 %) followed by NO_3 (18-20 %) and O_3 (8-12 %). At nighttime
the contribution from OH decreased to 43-53 %, and NO_3 increased to 26-40 % with that of O_3
largely unchanged. Of the measured $\sum$PANs, 48-78 % was modelled to be peroxyacetic nitric
anhydride (PAN). Physical loss (e.g. deposition) was an important sink for both ANs and PANs
and contributed significantly to the very short lifetimes of 1.5 ± 1 h for ANs and 0.08 - 1.5 h
for PANs observed during the campaign.

2   Introduction

Approximately 1000 Tg of biogenic volatile organic compounds (BVOCs) are emitted into the
atmosphere annually, whereof ~50% is isoprene and ~15% are monoterpenes (Guenther et al.,
2012). The oxidation of BVOCs is initiated by ozone (O_3) and the hydroxyl (OH) and nitrate
(NO_3) radicals. When BVOCs are oxidized in the presence of (largely anthropogenic) NO_x they
lead to the formation of alkyl nitrates ($RONO_2$, ANs) and peroxycarboxylic nitric anhydrides
($RC(O)O_2NO_2$, PANs) as illustrated in Figure 1. ANs are produced in the daytime in a minor
branch of the reaction between organic peroxy radicals (RO_2) which do not have an α-carbonyl
group and nitrogen oxide (NO, Lightfoot et al. (1992)) and through the reaction of unsaturated
BVOCs with NO_3 at nighttime. Recent studies suggest that the NO_3-initiated oxidation of
BVOCs during the day could also be an important pathway for the formation of alkyl nitrates
(Liebmann et al., 2019; Ayres et al., 2015; Liebmann et al., 2018a; Liebmann et al., 2018b;
Dewald et al., 2024). PANs are formed when α-carbonyl peroxy radicals ($RC(O)O_2$) react with
nitrogen dioxide (NO_2). The stability of PANs is highly temperature dependent resulting in
boundary layer lifetimes of the order of hours at temperate mid-latitudes with respect to
dissociation to $RC(O)O_2$ and NO_2 (Iupac, 2024).

The yield of alkyl nitrates in the RO_2 + NO reaction strongly depends on the composition of
BVOCs in the atmosphere, the oxidant that initiates the degradation of the BVOC (OH, O_3 or
NO_3), and the ratio of NO to other reactants with which the RO_2 can react such as NO_2, HO_2
and other RO_2 (Iupac, 2024; Perring et al., 2013; Wennberg et al., 2018; Hallquist et al., 1999;
Fry et al., 2014). The yield of the PANs formed from the corresponding α-carbonyl peroxy
radical depends only on the fraction of $RC(O)O_2$ that reacts with NO_2 as opposed to reacting
with HO_2 or NO. Production and loss processes of ANs and PANs are described in detail
through reaction mechanisms and equations in section 4.1-4.3 and 4.6, respectively.

The formation of ANs and PANs serves to sequester reactive nitrogen (NO_x = NO + NO_2) into
reservoir species, which can release NO_x following transport to regions remote from NO_x
sources; both can also be removed from the lowermost atmosphere through deposition, which
thus represents a sink of NO_x in the atmosphere. As NO_2 is formed from primary emitted NO
and its photolysis drives the formation of O_3, understanding the fate of NO_x is critical for
predicting O_3 levels in the troposphere. It has additionally been shown that ANs contribute

significantly to the rate of formation and growth of secondary organic aerosols (SOA) and thereby impacting human health and air quality (Hallquist et al., 2009; Shiraiwa et al., 2017; Kanakidou et al., 2005).

70

This study investigates the production and loss of PANs and ANs in an anthropogenically impacted temperate forest using field measurements of BVOCs, oxidants (OH, O_3, and NO_3), products (PANs and ANs), and meteorological data. The lifetimes of PANs and ANs are derived from their production rates and measured total mixing ratios.

75

3   Methodology

3.1   Site Description

The measurements used in this study were conducted at the Rambouillet forest site located approximately 50 km southwest of Paris, France, (48.687, 1.704) during the ACROSS
80   (Atmospheric ChemistRy Of the Suburban foreSt) campaign between June 13th 2022 and July 25th 2022 (Cantrell and Michoud, 2022). The forest consists of approximately 70% oak, 20% pine, and small contributions from beech and chestnut. The top of the forest canopy around the site was approximately 20-25 m. A 40 m measurement tower and multiple containers with a large variation in instruments were located in a clearing (~697 m^2). 48h HYSPLIT back
85   trajectories showed that the airmasses sampled during the campaign passed either over the Atlantic Ocean or Continental regions in Europe before reaching the site (Draxler and Rolph, 2011; Andersen et al., 2024). All the instruments used in this study are described briefly below.

3.2   Measurements
90   #### 3.2.1   Reactive Nitrogen and O_3
NO_2, total peroxycarboxylic nitric anhydrides ($\sum$PANs), total alkyl nitrates ($\sum$ANs), NO_3 reactivity (k^{NO3}), and O_3 were measured by instruments inside the MPIC (Max Planck Institute for Chemistry) container with co-located inlets sampling from a high-volume-flow stainless steel tube (10 m^3 min^{-1}; 15 cm diameter, 0.2 s residence time) taking air from a height of 5.4 m
95   above ground.

A 5-channel thermal dissociation cavity-ringdown spectrometer (5CH-TD-CRDS, Sobanski et al. (2016)) was used to measure NO_2, $\sum$PANs, and $\sum$ANs. NO_2 was measured directly at 408 nm with a limit of detection (LOD) of 9.7 parts per trillion by volume (pptv) for 1 min averaging (3σ). $\sum$PANs and $\sum$ANs were thermally dissociated to NO_2 by heating their separate
100   inlets to 448 and 648 K, respectively, followed by detection of NO_2 at 408 nm. Numerical simulations were run for both $\sum$PANs and $\sum$ANs to correct for NO_2 loss via recombination with RO_2, the reactions of peroxy radicals with ambient NO, NO oxidation to NO_2 by O_3, and pyrolysis of O_3 (Thieser et al., 2016; Sobanski et al., 2016). The majority of the correction factors for both $\sum$PANs and $\sum$ANs were between 0.9 and 1.2 as shown in Figure S1, which is
105   consistent with low NO_x levels. Two additional cavities, operated at 662 nm, measured NO_3 and (via thermal dissociation to NO_3, 373 K) N_2O_5 (Sobanski et al., 2016). A timeseries of NO_2, $\sum$PANs, and $\sum$ANs is shown in Figure 2.

A second CRDS-instrument was used to primarily measure the NO_3 reactivity towards VOCs (k^{NO3}) in the forest, but it also has a cavity operated at 405 nm for the measurement of NO_2

(Liebmann et al., 2018b). The ambient NO_3 reactivity is quantified by a CRDS-measurement (at 662 nm) of in-situ-generated NO_3 after its residence in a flow-tube reactor when mixed with either synthetic or ambient air. A numerical simulation procedure is used to correct the measurements for competing reactions taking place inside the flow-tube in order to extract the VOC contribution to the measured NO_3 consumption. A detailed analysis of the NO_3 reactivity measurements is presented in Dewald et al. (2024). During the ACROSS campaign, the reactivity of NO_3 towards organics was dominated by those of biogenic origin, so henceforth we refer to this as k^{BVOC}.

O_3 was measured with a commercial instrument (2B Technologies model 205) using UV absorption at ~254 nm. The LOD is 2 ppbv for 10 s averaging time. A timeseries of O_3 can be observed in Figure 2.

NO was measured using a commercial chemiluminescence instrument (Ecophysics CLD 780 TR, henceforth CLD) with an LOD of 10 pptv for 1 min averaging time. The sampling height for NO measurements was about 3.2 m above the ground surface and the inlet was approximately 17 m from the MPIC container. The NO measurements were corrected as described in (Andersen et al., 2024).

3.2.2   OH and XO_2 (HO_2+RO_2)

The OH radical was measured by its conversion (via reaction with isotopically labelled SO_2) to H_2SO_4 which was subsequently detected using nitrate chemical ionization mass spectrometry (Eisele and Tanner, 1991). The lower limit of detection for OH radicals at signal-to-noise-ratio (S/N)=3 and a 15-minute integration time was 5×10^4 molecule cm^{-3}. The sum of peroxy radicals, XO_2=HO_2+RO_2, was measured by their conversion to OH in the presence of NO. The OH calibration coefficient was determined using N_2O actinometry and OH generation in a turbulent flow reactor by photolysis of N_2O or H_2O at 184.9 nm (Kukui et al., 2008). The calibration of HO_2, CH_3O_2 and other RO_2 was performed by adding into the calibration reactor CO, CH_4 (or other RO_2 precursors) converting OH to RO_2. The overall estimated calibration accuracy (2σ) for OH is about 25% and about 30% for calibrated XO_2, although the uncertainty of the XO_2 measurements is typically higher due to variable detection efficiency (i.e. yields of OH) of different XO_2. The lower limit of detection for XO_2 radicals at S/N=3 and a 4-minute integration time is 2×10^6 molecule cm^{-3}. A detailed description of the instrument and calibration system are presented elsewhere (Kukui et al., 2008; Kukui et al., 2021). During the ACROSS field campaign the instrument was installed in a shipping container with the chemical conversion reactor fixed to the roof of the container via an interface cap covered with a polytetrafluoroethylene (PTFE) sheet. The sampling aperture of the chemical conversion reactor (3 mm diameter) was positioned 50 cm above the roof and about 3 m above the ground surface. A detailed analysis of the OH measurements will be presented in a forthcoming publication.

3.2.3   Photolysis frequencies and meteorology

A spectral radiometer (metcon Gmbh) was installed near the high-volume-flow stainless-steel tube on top of the MPIC container to measure actinic fluxes, which were converted to photolysis frequencies using recommended absorption spectra and quantum yields (Iupac, 2024; Burkholder et al., 2020) as described in Meusel et al. (2016). Note that upwelling

155 Ambient temperature was measured at four different heights on the tower; 5 m, 13 m, 21 m,
and 41 m using temperature sensors from Atexis (PT1000) and Thermoest (PT100). Relative
humidity was measured at 5 m using a Vaisala humidity sensor (HMP45A).

3.2.4 Biogenic Volatile Organic Compounds (BVOCs)

160 The LISA Proton Transfer Reaction Time of Flight Mass Spectrometer (PTR-ToF-MS,
hereafter called PTRMS), manufactured by Kore Technology Ltd., was used for monitoring
concentrations of VOCs. Air samples were drawn at a flow rate of approximately 300 mL min^{-1}
through a 3 m long Silcosteel® coated stainless steel tube (2.1 mm inner diameter).
Calibration was performed approximately every 3 days using VOC standards (5 – 20 ppb) from
165 a certified National Physical Laboratory (NPL) calibration mixture with nominally 1 ppmv
±5% of several trace gases including acetaldehyde, methanol, ethanol, isoprene, acetone,
dimethyl sulphide, acetonitrile, 3-carene. Humidity corrections were applied for each trace-
gas. Mixing ratios of non-calibrated trace gases were retrieved from reactor conditions, rate
constants, fragmentations, and ion transmissions determined using the same NPL standard
170 cylinder. The time series of acetaldehyde, isoprene and total monoterpenes ($\sum$MT) is shown in
Figure 2.

As there were no measurements of speciated monoterpenes, due to instrumental issues with the
gas chromatography instrument deployed during the campaign, different potential
monoterpene mixtures were determined using the total mixing ratios measured by the PTRMS
175 together with the measured reactivity of NO$_3$ towards BVOCs (k^{BVOC}) after subtracting the
reactivity due to isoprene as described in Eq. (1). Here, $k_{\text{effective}}$ is an effective rate coefficient
for the reaction of NO$_3$ with an assumed monoterpene mixture. $k_{\text{effective}}$ was determined by
adding all the fractional contributions from different monoterpenes as described in equation
(2), where a$_i$ and $k_{\text{NO3}+i}$ are the fractional contribution and the rate coefficient with NO$_3$ for
180 monoterpene i, respectively, which are listed in Table 1.

$$[\textstyle\sum\text{Monoterpenes}] = \frac{k^{\text{BVOC}} - k_{\text{NO3+isoprene}}[\text{Isoprene}]}{k_{\text{effective}}} \qquad (1)$$

$$k_{\text{effective}} = \textstyle\sum_i (a_i \times k_{\text{NO3}+i}) \qquad (2)$$

Only limonene, α-pinene, and β-pinene were used to determine potential mixtures since the
box-model used (see below) contained schemes for their degradation only. By varying
185 limonene between 10 and 30% of the sum of monoterpenes ($\sum$MT) three potential mixtures
which were consistent with the measured NO$_3$-reactivity were determined. Mixture 1: 30%
limonene, 10% β-pinene, and 60% α-pinene. Mixture 2: 20% limonene, 15% β-pinene, and
65% α-pinene. Mixture 3: 10% limonene, 5% β-pinene, and 85% α-pinene. All three scenarios
are plotted together with the measured $\sum$MT over a 48-hour period in Figure 3B. Here the three
190 scenarios can be observed to agree well with the measurements except when a temperature
inversion occurred (Figure 3A). The same kind of discrepancy is observed every night with a
temperature inversion, which is shown in Figure 3C, where mixture 2 is plotted against the
measured $\sum$MT for the entire campaign and coloured by the difference in temperature (ΔT)
between the top of the tower (41 m) and measurement height (5m). A significant temperature

inversion can result in the formation of a shallow nocturnal surface layer with weak vertical mixing.

As BVOCs continue to be emitted at night, weak vertical mixing leads to a strong gradient in monoterpene mixing ratios with higher values at low heights above ground level. As the gradient (both horizontally and vertically) will depend on the lifetime of each monoterpene, the mixture of monoterpenes measured by the NO_3-reactivity instrument (at 5.4 m) might not be the same as that emitted by the vegetation at different heights. In Figure S2, the average derived diel profiles of the lifetime of α-pinene, β-pinene, and limonene when taking reactions with OH, O_3, and NO_3 into account using the rate coefficients in Table 1 are plotted. During the daytime all three monoterpenes have short lifetimes of around 0.5-1.5 hours; however, at nighttime, limonene clearly has the shortest lifetime, whereas β-pinene has a slightly longer lifetime than α-pinene. On nights with ΔT>1°C, limonene is therefore assumed not to be sampled by the NO_3-reactivity instrument due to the slow vertical and horizontal mixing and the monoterpene mixture is changed to 57% β-pinene and 43% α-pinene, which can be seen in Figure 3D for scenario 2. This correction aligns the calculated and measured ∑MT throughout the entire campaign (Figure 3E).

3.3 Box Model

To simulate PANs numerically, we have used the atmospheric chemistry box model CAABA/MECCA (Chemistry As A Boxmodel Application/Module Efficiently Calculating the Chemistry of the Atmosphere) by Sander et al. (2019). The code is based on model version 4.7.0, and it has been adapted to simulate the ACROSS campaign. To allow for a detailed calculation of monoterpenes and PANs, reactions were exported from the Master Chemical Mechanism (MCM, https://mcm.york.ac.uk), including the MCM species APINENE, BPINENE, C_3H_8, C_5H_8, CH_3CHO, CH_4, LIMONENE, and NC_4H_{10} in the marklist. This resulted in a gas-phase chemical mechanism with 1536 species and 4550 reactions. The setup of the individual model runs will be described in Sect. 4.7.

4 Results and Discussion

4.1 AN production from NO_3 reactions with BVOCs

NO_3 radicals are produced from the reaction between NO_2 and O_3 (R1) and are usually lost rapidly during daytime to photolysis and reactions with unsaturated BVOCs and NO (R2-R4). Reactions between NO_3 radicals and unsaturated BVOCs lead to the formation of alkyl nitrates (ANs, R3a) as well as other products (R3b). At nighttime, ground-level NO_3 mixing ratios can vary greatly from < 1 pptv to > 100 pptv depending on atmospheric composition (Ng et al., 2017; Brown and Stutz, 2012), i.e. their production and loss terms. During ACROSS, the NO_3 reactivity within the canopy was generally high at nighttime due to the emission of biogenic volatile organic compounds (BVOCs, by vegetation) and NO (from soil) into a shallow, poorly mixed nocturnal surface layer (Dewald et al., 2024; Andersen et al., 2024). This led to NO_3 mixing ratios, at the ground, of < 0.5 pptv, which were generally lower than the limit of detection of instrumentation at the site.

$$NO_2 + O_3 \rightarrow NO_3 + O_2 \qquad\qquad\qquad (R1)$$

$$NO_3 + h\nu \rightarrow NO_2 + O \tag{R2a}$$

$$NO_3 + h\nu \rightarrow NO + O_2 \tag{R2b}$$

$$NO_3 + BVOC \ (O_2, NO, RO_2, HO_2) \rightarrow ANs \tag{R3a}$$

240
$$NO_3 + BVOC \rightarrow other\ products \tag{R3b}$$

$$NO_3 + NO \rightarrow 2\ NO_2 \tag{R4}$$

The total production rate of ANs from the NO_3-initiated oxidation of unsaturated BVOCs can be calculated using equation (3), where $[NO_3]_{SS}$ is the NO_3 concentration at steady state and $\alpha_i^{NO_3}$, $k_i^{NO_3}$ and $[C_i]$ are the ANs yield, the rate coefficient and BVOC concentration for

245 compound i, respectively. $[NO_3]_{SS}$ is determined from the production and loss terms described by reactions (R1-R4) as described in equation (4), where [NO], [NO$_2$], and [O$_3$] are the concentrations of NO, NO$_2$, and O$_3$, respectively, k_1 and k_4 are the rate coefficients of reaction (R1) and (R4), respectively, k^{BVOC} is the first-order loss frequency for NO_3 towards BVOCs, and J_{NO3} is the photolysis frequency of NO_3 radicals (Liebmann et al., 2019). This calculation

250 ignores physical losses of NO_3 (e.g. deposition) which will not compete with its reactive losses in this environment.

$$\sum P_{ANs}^{OH} = [NO_3]_{SS} \sum_i \alpha_i^{NO_3} k_i^{NO_3} [C_i] \tag{3}$$

$$[NO_3]_{SS} = \frac{k_1[NO_2][O_3]}{k^{BVOC} + J_{NO3} + k_4[NO]} \tag{4}$$

255 **4.2 AN production from OH reactions with BVOCs**

At daytime, primary OH radicals are produced e.g. from the photolysis of O$_3$ followed by the reaction between O(^{1}D) and water vapour (R5-R6) with secondary production through reaction of HO$_2$ (formed in peroxy-radical (RO$_2$) reactions) with NO. In the absence of photochemistry, OH concentrations are generally lower at nighttime than at daytime, with average hourly

260 concentrations of around 3.5-5 $\times$ 10^5 molecules cm^{-3} observed across the campaign. The nighttime OH results from the ozonolysis of unsaturated BVOCs (see below) in the nocturnal boundary layer, which was very shallow and stable due to temperature inversions (Andersen et al., 2024). When OH reacts with BVOCs in the presence of O$_2$, peroxy radicals are produced (R7), which can then react with NO to give alkyl nitrates (R8a), as well as alkoxy radicals and

265 NO$_2$ (R8b). Additional competing processes that lower the yield of ANs from RO$_2$ are reactions with itself and other RO$_2$ (R9) and reaction with HO$_2$ (R10).

$$O_3 + h\nu \rightarrow O(^1D) + O_2 \tag{R5}$$

$$O(^1D) + H_2O \rightarrow 2\ OH \tag{R6}$$

$$OH + BVOC \ (+O_2) \rightarrow RO_2 + H_2O \tag{R7}$$

270
$$RO_2 + NO + M \rightarrow RONO_2 + M \tag{R8a}$$

$$RO_2 + NO \rightarrow RO + NO_2 \tag{R8b}$$

$$RO_2 + RO_2 \rightarrow products \tag{R9}$$

$$RO_2 + HO_2 \rightarrow ROOH + O_2 \tag{R10}$$

275 The total production rate of ANs from OH-initiated oxidation of BVOCs is described in equation (5), where [OH] is the OH concentration, $\alpha_i^{RO_2}$ is the fraction of the organic peroxy radicals from BVOCs which (via R8a) forms an alkyl nitrate when reacting with NO, k_i^{OH} and $[C_i]$ are the rate coefficient and BVOC concentration for compound i, respectively, and β is the fraction of peroxy radicals that reacts with NO (rather than RO_2 or HO_2) as described in equation (6) (Liebmann et al., 2019). It was calculated using the measured XO_2 and NO

280 together with a generic rate coefficient for reaction (R8), 8×10^{-12} cm^3 molecule^{-1} s^{-1}, and a combination of reactions (R9) and (R10), 1×10^{-11} cm^3 molecule^{-1} s^{-1} (Iupac, 2024).

$$\sum P_{ANs}^{OH} = [OH]\beta \sum \alpha_i^{RO_2} k_i^{OH}[C_i] \tag{5}$$

$$\beta = \frac{k_8[NO]}{k_8[NO] + k_9[RO_2] + k_{10}[HO_2]} \tag{6}$$

4.3 AN production from O$_3$ reactions with BVOCs

285 Ozone (O$_3$) addition to an unsaturated BVOC forms a primary ozonide (POZ, R11), which in the presence of O$_2$ can rapidly decompose via Criegee intermediates to OH and organic peroxy radicals (RO$_2$) (R12a). The POZ can also react through other processes that do not result in organic peroxy radicals (R12b). The RO$_2$ formed in (R12a) further reacts through reactions

290 (R8-R10) as described above.

$$O_3 + R=R \rightarrow POZ \tag{R11}$$

$$POZ (+O_2) \rightarrow OH + RO_2 \tag{R12a}$$

$$POZ \rightarrow other\ products \tag{R12b}$$

Equation (7) describes the total production rate of ANs from the O$_3$-initiated oxidation of

295 unsaturated BVOCs, where [O$_3$] is the O$_3$ concentration, $\alpha_i^{O_3}$ is the yield of RO$_2$ from reactions (R11-R12a), $\alpha_i^{RO_2}$ is the fraction of the organic peroxy radicals (from BVOCs) formed in (R12a) which when reacting with NO form an alkyl nitrate, $k_i^{O_3}$ and $[C_i]$ are the rate coefficient and BVOC concentration for compound i, respectively, and β is the fraction of peroxy radicals that react with NO as described in equation (6) (Liebmann et al., 2019), calculated as described

300 in section 4.2. Here we assume that the yield of ANs from RO$_2$ + NO is independent of whether RO$_2$ is formed by OH or O$_3$-initiated oxidation.

$$\sum P_{ANs}^{O_3} = [O_3]\beta \sum_i \alpha_i^{O_3} \alpha_i^{RO_2} k_i^{O_3}[C_i] \tag{7}$$

4.4 Relative importance of OH, O$_3$ and NO$_3$ oxidation for the production of ANs

305 To analyse the production and loss processes of alkyl nitrates during the ACROSS campaign, the measurements have been separated into two phases: phase 1 (lower photochemical activity) from June 28th 2022 to July 7th 2022, and phase 2 (higher photochemical activity) from July 8th 2022 to July 20th 2022. Average diel profiles of O$_3$, NO$_2$, NO, temperature, OH radicals, and isoprene for the two phases are plotted in Figure 4. Phase 1 is characterised by low levels of

310 oxidants and organics and a maximum average daytime temperature around 25 degrees Celsius,

whereas phase 2 is characterised by higher levels of oxidants and organics due to generally higher temperatures (maximum average daytime temperature around 30 degrees Celsius). The average monoterpene mixtures for the two phases are displayed in Figure 5 for mixture 2 with 20% limonene, 15% β-pinene, and 65% α-pinene. The monoterpene mixtures derived for
315 scenario 1 and 3 are plotted in Figure S3. At daytime the average mixture reflects the percentages used for each scenario, whereas at nighttime, the mixture is dominated by β-pinene and α-pinene during both phases, associated with temperature inversions.

The diel profile of the $\sum$ANs production rates from NO_3-, OH-, and O_3-initiated oxidation for mixture 2 using the rate coefficients and yields in Table 1 and the monoterpene mixture in
320 Figure 5 is shown in Figure 6A and B for phases 1 and 2, respectively. The total ANs production during phase 1 is fairly constant at 35-75 pptv h^{-1} throughout the diel profile. In contrast, phase 2 shows large variation with 80-100 pptv h^{-1} in the early morning between 01:00-05:00 UTC (03:00-07:00 LT) and 220-280 pptv h^{-1} around late morning to midday between 07:00-12:00 UTC (09:00-14:00 LT). For both phases, the variability in the $\sum$ANs production rate from O_3
325 and NO_3-initiated oxidation of BVOCs is small. The calculated averaged O_3-initiated $\sum$ANs production rate is 9 ± 3 and 18 ± 4 ($\pm 1\sigma$) pptv h^{-1} for phase 1 and 2, respectively, and the derived averaged NO_3-initiated $\sum$ANs production rate is 12 ± 5 and 41 ± 11 ($\pm 1\sigma$) pptv h^{-1} for phase 1 and 2, respectively. The differences between the two phases are therefore caused by the OH-initiated oxidation, which is relatively stable during phase 1 at 34 ± 11 ($\pm 1\sigma$) pptv h^{-1}
330 on average due to the lower daytime levels of OH and BVOCs (see Figure 4), but varies between 30-70 pptv h^{-1} at nighttime and 100-230 pptv h^{-1} at daytime during phase 2.

Figure 6C and D show the fractional contributions of NO_3-, OH-, and O_3-initiated oxidation (mixture 2) to the $\sum$ANs production rate for phase 1 and 2, respectively. OH clearly dominates at daytime (06:00-18:00 UTC) with, on average, 69-72 % for both phases, followed by NO_3
335 with 18-20 % and O_3 with 8-12 %. At nighttime (18:00-06:00 UTC), the picture is not as clear: During phase 1 OH-initiated oxidation is still the dominant ANs production pathway with, on average, 53 % and the remainder is close to evenly split at 21 and 26 % between O_3- and NO_3-initiated oxidation, respectively. At nighttime during phase 2, OH- and NO_3-initiated oxidation contributed similarly with 43 and 40 % of the total ANs production rate, respectively, leaving
340 only 17 % for O_3-initiated processes. The differences between the two phases at nighttime can be explained by the availability of the precursors, where there is approximately double the amount of O_3 and NO_2 during phase 2, leading to a higher production rate of NO_3 radicals and thereby an increased ANs production rate from NO_3-initiated oxidation.

Both phases give significantly different fractions at both daytime and nighttime to those
345 observed by Liebmann et al. (2019) in a boreal forest, where, in the absence of measurements, OH was calculated from the actinic flux, which thus resulted in zero OH at nighttime. However, both studies agree on NO_3 oxidation being a significant source of ANs, both at daytime and nighttime. If $[NO_3]_{SS}$ was calculated using photolysis frequencies measured above the clearing instead of inside the clearing, the contribution from NO_3-initiated oxidation would be reduced
350 in the morning and evening.

4.5 ANs loss and lifetime
Neglecting the role of transport, we now combine the diel profile of the total production rate of ANs (described above) with the average measured diel profile of ANs to evaluate the loss

355   processes and lifetime of the ANs using equation (8). P_{ANs} is the production rate of ANs, $[ANs]_0$ is the average ANs mixing ratio at 00:00 UTC, and $k_L(ANs)$ is the loss rate of the ANs, which is defined as the inverse of the lifetime of the ANs $((\tau_{ANs})^{-1})$.

$$\frac{d[ANs]}{dt} = P_{ANs} - k_L(ANs)[ANs]_0 \qquad (8)$$

The ANs mixing ratio at any subsequent time to $[ANs]_0$ can then be calculated as described in
360   Eq. (9) with the variation of $k_L(ANs)$ to match the observed ANs mixing ratio.

$$[ANs]_t = \int_0^t \frac{d[ANs]}{dt} + [ANs]_0 \qquad (9)$$

Figure 6E and F show the average diel profiles of the measured ANs in black for phase 1 and 2, respectively. The orange lines show how the ANs mixing ratios would have increased if there was no chemical or transport-induced loss throughout the day and the blue lines show
365   how the diel profiles would look when applying lifetimes of 1-10 hours for the ANs. The best fit to the measured diel profile of ANs results from using an effective lifetime in the clearing of 1.5 ± 1 h throughout the diel cycle for both phases despite the very different production rates described above. Table 2 gives an overview of the average daytime and nighttime loss rate frequencies and the resulting effective lifetimes. No difference was observed between daytime
370   and nighttime during phase 1 and only a small difference within the uncertainties was observed during phase 2.

The total ANs production rate resulting from the three different monoterpene mixtures derived above, plotted in Figure S4A for the two phases, clearly shows that the choice of mixture does not have a significant impact on the total production rate. This means that the determined
375   lifetime for the two phases of 1.5 ± 1 h is consistent across all three mixtures, as can be observed in Figure S4C. This lifetime is similar to the 2 ± 3 h estimated in a boreal forest (Liebmann et al., 2019).

In section 4.7, it is shown that the box model described above predicts the mixing ratio of XO_2 to be up to 4 times higher than the measured XO_2 depending on the day. As the origin of this
380   model-observation discrepancy is not known we have calculated the total ANs production rate and the lifetime of ANs for the three monoterpene mixtures when applying 4 times the measured XO_2. The results (Figures S4B and S4D) show that β and thus P_{ANs} decrease when increasing XO_2, which results in an increase in the calculated lifetime from 1.5 ± 1 h to 2.5 ± 1.5 h, which remains consistent with the previous measurements conducted in a boreal forest.

385

4.6   PANs major production and loss processes
A dominant fraction of the measured PANs is expected to be in the form of peroxyacetic nitric anhydride ($CH_3C(O)O_2NO_2$, PAN), which is formed in the reaction between the peroxyacetyl radical ($CH_3C(O)O_2$) and NO_2 (R13). In the boundary layer, $CH_3C(O)O_2$ is produced directly
390   from the OH-initiated oxidation of acetaldehyde (CH_3CHO, R14) and the photolysis of dicarbonyls such as methylglyoxal ($CH_3C(O)CHO$, R15, Crowley et al. (2018)) and from the oxidation of BVOCs such as isoprene (via methacrolein ($CH_2C(CH_3)CHO$, MACR) and methyl vinyl ketone ($CH_2CHC(O)CH_3$, MVK)) and α-pinene after multiple reaction steps.

$$CH_3C(O)O_2 + NO_2 \qquad \rightarrow \qquad CH_3C(O)O_2NO_2 \text{ (PAN)} \qquad (R13)$$

395	OH + CH$_3$CHO + O$_2$	$\rightarrow$ CH$_3$C(O)O$_2$ + H$_2$O	(R14)
	CH$_3$C(O)CHO + $h\nu$ + 2 O$_2$	$\rightarrow$ CH$_3$C(O)O$_2$ + CO + HO$_2$	(R15)
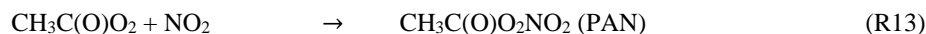
In the summertime, forested environments, where isoprene emissions are high, peroxymethacrylic nitric anhydride (CH$_2$C(CH$_3$)C(O)O$_2$NO$_2$, MPAN), an OH-initiated oxidation product of MACR (R16-R17), is expected to make a significant contribution to the total peroxy nitrates. With an annual average propane (C$_3$H$_8$) measurement around 507 pptv at La Tardiere, France, in 2018 (Ge et al., 2024), peroxypropionic nitric anhydride (CH$_3$CH$_2$C(O)O$_2$NO$_2$, PPN), an OH-initiated oxidation product of propanal (CH$_3$CH$_2$CHO, R18-R19), is expected to be present as well.

	OH + CH$_2$C(CH$_3$)CHO (MACR) + O$_2$	$\rightarrow$	CH$_2$C(CH$_3$)C(O)O$_2$ + H$_2$O	(R16)
405	CH$_2$C(CH$_3$)C(O)O$_2$ + NO$_2$	$\rightarrow$	CH$_2$C(CH$_3$)C(O)O$_2$NO$_2$ (MPAN)	(R17)
	OH + CH$_3$CH$_2$CHO + O$_2$	$\rightarrow$	CH$_3$CH$_2$C(O)O$_2$ + H$_2$O	(R18)
	CH$_3$CH$_2$C(O)O$_2$ + NO$_2$	$\rightarrow$	CH$_3$CH$_2$C(O)O$_2$NO$_2$ (PPN)	(R19)
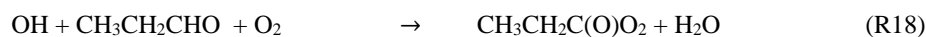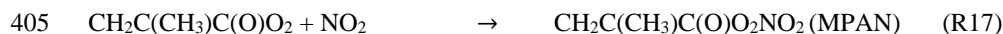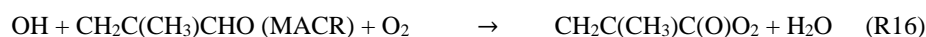
For both PAN, MPAN, PPN and any other PANs, the production rate strongly depends on the presence of NO, hydroperoxyl radicals (HO$_2$) and other peroxy radicals (RO$_2$) that can lead to competing reactions (R20-R21) to (R13), (R17) and (R19). XO$_2$ describes the sum of HO$_2$ + RO$_2$.

	RC(O)O$_2$ + NO	$\rightarrow$	R + CO$_2$ + NO$_2$	(R20)
	RC(O)O$_2$ + XO$_2$	$\rightarrow$	RC(O)O + XO + O$_2$	(R21)

PANs are permanently removed through deposition (R22) and can be lost through thermal decomposition (R23) reforming RC(O)O$_2$, which can subsequently react as described above (R20-R21). Larger and/or unsaturated PANs, such as MPAN, can also be lost through oxidation (R24).

	RC(O)O$_2$NO$_2$	$\rightarrow$	Deposition	(R22)
	RC(O)O$_2$NO$_2$	$\rightarrow$	RC(O)O$_2$ + NO$_2$	(R23)
420	RC(O)O$_2$NO$_2$ + OH	$\rightarrow$	Products	(R24)
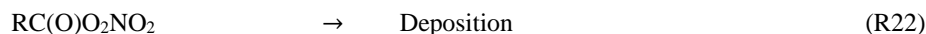
The thermal decomposition of PANs is strongly temperature dependent resulting in lifetimes with respect to (R23) of 7.5 hours at 283 K and 40 minutes at 298 K (Iupac, 2024). The effective lifetime increases from that calculated from the thermal decomposition rate coefficient when regeneration of PANs through e.g. reaction (R13), (R17), and (R19) occurs. Thermal decomposition is thus expected to be the dominant loss process of PANs at high temperatures in the presence of NO and/or XO$_2$, however, at nighttime, when the temperature is lower and the mixing ratios of NO and XO$_2$ also are lower, deposition can play an important role depending on boundary layer height, humidity and surfaces.

4.7 Measured and modelled PANs

Figure 7A plots the mixing ratio for ΣPANs for which maximum daytime mixing ratios are between 100 pptv and 1600 pptv. The large variability is presumably caused by the observed

variability in temperature, concentrations of oxidants, and BVOCs. The temperature fluctuations measured during the campaign results in a thermal lifetime of the PANs that spans two orders of magnitude from 15 hours at 279 K and 3 minutes at 314 K (the extremes measured during ACROSS) as shown in Figure 7B.

Due to the many different production pathways of PANs, we used a detailed chemical box-model (see section 3.3 for details) to assess the contributions of various precursors and compare to measured ∑PANs. As the calculated thermal loss rate varies significantly from day to day, two single days (marked in grey in Figure 7) where measurements of OH, O_3, NO, NO_2, and BVOCs are available have been modelled instead of using average diel profiles like in the ANs analysis. One day (July 4th 2022) is in phase 1 from the ANs analysis, where the temperature reaches around 27°C (300 K) resulting in a thermal lifetime of 25 minutes (without considering recombination) and during which the mixing ratios of precursors (oxidants and BVOCs) were low. The second day (July 13th 2022) is in phase 2 from the ANs analysis, where the temperature has a maximum of around 39°C (312 K) resulting in a thermal lifetime of around 5 minutes (without considering recombination) and higher precursor levels than during the first day.

The box model was constrained by measurements (10-minute running averages) of temperature, OH, O_3, NO, NO_2, isoprene, and acetaldehyde (CH_3CHO), and the estimated monoterpene mixture of α-pinene, β-pinene, and limonene as described above for the case with 20% limonene. Note that varying the fraction of limonene did not change the modelled ∑PANs significantly. The model was additionally initiated using average CO and pressure for the modelled day and 507 pptv propane (C_3H_8), 193 pptv n-butane (n-C_4H_{10}), and 107 pptv isobutane (i-C_4H_{10}) (Ge et al., 2024). To ensure that all the trace gases not constrained in the model were in steady-state, a spin-up time of nine days was used. The thermal losses of PANs were included in the model as described above and an additional first-order loss term (physical losses from e.g. deposition) was varied to get satisfactory model-measurement agreement for ∑PANs during daytime (06:00-18:00 UTC) and nighttime (18:00-06:00 UTC) for the individual days. The physical loss frequencies thus derived were at daytime 5.5×10^{-4} s^{-1} and 2.6×10^{-3} s^{-1} for the low and high precursor day, respectively, and 1.8×10^{-4} s^{-1} and 1.1×10^{-3} s^{-1} at nighttime. There are several potential explanations for the enhanced physical loss of PANs at daytime compared to nighttime. The daytime increase could be explained by a reduction in the surface resistance to foliar uptake when plant-stomata are open, (similar to O_3, Shepson et al. (1992)) or a reduction in the transport resistance to uptake due to turbulent mixing. Rapid vertical mixing (venting) out of the canopy would also contribute to the net physical losses during daytime (Bohn, 2006) if significant concentration gradients exist. However, as effects of venting were not observed for alkyl nitrates (i.e. no significant difference between physical loss frequency during day and night was observed), we do not consider venting to be significant.

According to the model, at daytime (06:00-18:00 UTC, 08:00-20:00 LT), PAN contributes 61-78 % and 58-72 % of ∑PANs for the low and high precursor day, respectively. The nighttime PAN contribution to the ∑PANs is lower at 48-70 % and 48-60 %, respectively. The lower contribution of PAN to ∑PANs at nighttime is related to the high nighttime mixing ratios of monoterpenes (caused by the vegetation emitting BVOCs into a shallow boundary layer), which degrade to form larger PANs (see Table S1) compared to PAN. During the BEARPEX-2007 campaign in the Sierra Nevada Mountains, PAN was determined at local noon time to

contribute 70-90 % of ∑PANs (Wolfe et al., 2011), which is in reasonable agreement with our daytime results. A list of the modelled PANs is given in Table S1.

480 The model generated high amounts of HPAN (HOCH$_2$C(O)O$_2$NO$_2$) from glycolaldehyde, despite HPAN having a very short thermal lifetime (Zheng et al., 2011) and never having been detected in ambient air samples. In order to reduce the modelled contribution of HPAN to ∑PANs, an arbitrary loss term (10 times that of the other PANs) was included in the model.

The modelled PANs, separated into PAN and other PANs when optimized for nighttime are
485 plotted for the low and high precursor day in Figure 8A and B together with the measured mixing ratios. Reasonable agreement between the measured and modelled ∑PANs can be observed for both the high and low precursor day at nighttime and from 12:00-18:00 UTC when optimizing for nighttime agreement. However, the model overestimates the measurement between 06:00 and 12:00 UTC on both days by up to a factor of 4. When optimizing for daytime
490 agreement in the model (see Figure S5A and B) reasonable agreement can be observed between 06:00-18:00 for the high precursor day. For the low precursor day, the model overestimates the measurement between 06:00 and 12:00 UTC and underestimates between 12:00 and 18:00 UTC. For both days optimizing for daytime agreement by adjusting the ∑PANs physical loss term using a constant value for the whole day results in a significant underestimation of
495 modelled ∑PANs compared to the measured at nighttime. The lower nighttime physical loss results from temperature inversions and weak vertical mixing.

The loss of PAN is caused by a combination of physical losses such as deposition, and (at daytime) transport and thermal decomposition, which are plotted together in Figure 9C and D. In this case, the physical losses (modelled as a single loss frequency) were adjusted to optimize
500 measurement-model agreement at nighttime. To calculate an effective thermal loss rate coefficient, a correction factor which takes recombination through for example reaction (R13) into account was applied. The correction factor is described in equation (10) and represents the fraction of RC(O)O$_2$ formed from the thermal decomposition that does not lead to reformation of PANs.

505 $$f_{\mathrm{NO2}} = 1 - \left(\frac{k_{\mathrm{RC(O)O2+NO2}}[\mathrm{NO_2}]}{k_{\mathrm{RC(O)O2+NO2}}[\mathrm{NO_2}]+k_{20}[\mathrm{NO}]+k_{21}[\mathrm{XO_2}]} \right) \qquad (10)$$

where k_i is the rate coefficient for reaction (Ri), and [NO$_2$], [NO], and [XO$_2$] are the concentrations of NO$_2$, NO, and XO$_2$ (HO$_2$+RO$_2$). In the box model, NO and NO$_2$ are constrained to the measurements whereas XO$_2$ is calculated. The modelled XO$_2$ is compared to the measured value in Figure S6 for the two chosen days. On the low precursor day, the
510 model and measurements agree well, but on the high precursor day, the model predicts that XO$_2$ should be 4 times higher than the measurements at midday. The effective thermal decomposition rate coefficient for PAN (considering recombination of CH$_3$C(O)O$_2$ with NO$_2$, see above) is therefore shown using both the measured and the modelled XO$_2$. If the measured XO$_2$ is correct (and the modelled values are too high on the day during phase 2), the modelled
515 derived physical loss frequency would be too low and would have to be incremented by the difference in effective thermal decomposition frequencies (approximately 5×10^{-4} s^{-1}).

Thermal decomposition accounts for approximately 40 % of the total loss when using modelled XO$_2$ and optimizing for daytime agreement (see Figure S4C and D). Table 2 shows an overview of the average modelled thermal, physical, and total loss frequencies of PANs at daytime and

520 nighttime and the resulting effective lifetimes. The nighttime effective lifetime for ∑PANs during the low photochemical activity day was similar to that determined for ANs with 1.5 ± 0.1 h, but the daytime effective lifetime was significantly shorter with 0.42 ± 0.05 h. On the day with high photochemical activity, the average effective lifetime was even shorter at 0.08 ± 0.01 and 0.24 ± 0.02 h for daytime and nighttime, respectively. The total loss frequency peaked

525 at 0.0038 s^{-1} and 0.00085 s^{-1} for the high and low photochemical activity days resulting in effective lifetimes of around 4.4 min (0.07 h) and 20 min (0.32 h), respectively, when adjusting the physical loss frequency for measurement-model agreement at daytime.

5   Conclusion:

530 Measurements of NO_x, O_3, BVOCs, the sum of alkyl nitrates (∑ANs), and the sum of peroxycarboxylic nitric anhydrides (∑PANs) have been used to analyse the sources, sinks and lifetime of ANs and PANs in a temperate forest influenced by anthropogenic emissions.

The ANs analysis has been performed for two phases. The first phase is characterised by relatively low temperatures, oxidants and reactant compared to the entire campaign, and the

535 second phase was characterised by higher temperatures, oxidants and reactants. This led to significantly different production rates, but very similar lifetimes. The production was dominated by OH-initiated reactions at midday for both phases, but large differences were estimated at nighttime. NO_3-initiated reactions play a similarly important role as OH at nighttime for the second phase, however, for the first phase OH still dominates at nighttime.

540 NO_3-initiated reactions have also been shown to be important at daytime despite the rapid photolysis. The lifetime for both phases was short at 1-4 hours, which agrees with a previous study in a forest environment.

For the PANs analysis, a box model was used to simulate two individual days; one in the first phase of the ANs analysis and one in the second phase. Two constant physical loss terms are

545 applied for each of the two days optimized to match the average daytime and nighttime mixing ratios. For the low precursor day (July 4th 2022), loss frequencies of 5.5×10^{-4} s^{-1} and 1.8×10^{-4} s^{-1} were used to align measurement and model for daytime and nighttime, respectively, while for the high precursor day (July 13th 2022) 2.6×10^{-3} s^{-1} and 1.1×10^{-3} s^{-1} were used. This resulted in lifetimes of around 20 min and 4 min at midday for the low and high precursor day,

550 respectively, where thermal decomposition contributed approximately 40 %. Peroxyacetic nitric anhydride (PAN) represents 48-78% of ∑PANs according to the box model, with the highest fractions predicted at daytime.

Lifetimes of organic nitrates in the forested environment are very short, with deposition, presumably to soil and foliar surfaces playing an important role in removing them from the gas

555 phase. Through emission of reactive organic trace gases, the forest ecosystem thus captures essential nitrogen-containing nutrients originating from anthropogenic sources and transfers them to the biosphere.

6   Data Availability:

560 All measurements from the ACROSS campaign including NO_x (Andersen and Crowley, 2023b; Xue et al., 2023), O_3 (Crowley, 2023), organic nitrates (Andersen and Crowley, 2023a),

NO$_3$ reactivity (Dewald and Crowley, 2023), BVOCs (Michoud et al., 2024), meteorological quantities (Denjean, 2023), OH (Kukui, 2023a), and peroxy radicals (Kukui, 2023b) can be found at https://across.aeris-data.fr/catalogue/ (last access: 31 August 2024).

565

7 Author contribution:

All authors contributed with measurements. Data analysis was conducted by STA with contributions from JNC. RS did the box modelling. CC and VM organized the field campaign with contributions from the individual group leads. STA and JNC developed the manuscript
570 with contributions from all authors.

8 Competing Interests:

The authors declare that they have no conflict of interest.

575 ## 9 Acknowledgements:

STA is thankful to the Alexander von Humboldt foundation for funding her stay at MPIC.

PD gratefully acknowledges the Deutsche Forschungsgemeinschaft (project "MONOTONS", project number: 522970430).

The ACROSS project has received funding from the French National Research Agency (ANR)
580 under the investment program integrated into France 2030, with the reference ANR-17-MPGA-0002, and it was supported by the French National program LEFE (Les Enveloppes Fluides et l'Environnement) of the CNRS/INSU (Centre National de la Recherche Scientifique/Institut National des Sciences de l'Univers). CNRS-INSU provides support to the PEGASUS platform as a national facility. Data from the ACROSS campaign and the PEGASUS facility are hosted
585 by the French national center for Atmospheric data and services AERIS.

10 References:

Andersen, S. T. and Crowley, J. N.: ACROSS_MPIC_RambForest_5ch-PNs-ANs_10min_L2 [dataset], https://doi.org/10.25326/706, 2023a.
590 Andersen, S. T. and Crowley, J. N.: ACROSS_MPIC_RambForest_5ch-NO2_1min_L2 [dataset], https://doi.org/10.25326/705, 2023b.
Andersen, S. T., McGillen, M. R., Xue, C., Seubert, T., Dewald, P., Türk, G. N. T. E., Schuladen, J., Denjean, C., Etienne, J. C., Garrouste, O., Jamar, M., Harb, S., Cirtog, M., Michoud, V., Cazaunau, M., Bergé, A., Cantrell, C., Dusanter, S., Picquet-Varrault, B.,
595 Kukui, A., Mellouki, A., Carpenter, L. J., Lelieveld, J., and Crowley, J. N.: Measurement report: Sources, sinks, and lifetime of NO$_x$ in a suburban temperate forest at night, Atmos. Chem. Phys., 24, 11603-11618, 10.5194/acp-24-11603-2024, 2024.
Ayres, B. R., Allen, H. M., Draper, D. C., Brown, S. S., Wild, R. J., Jimenez, J. L., Day, D. A., Campuzano-Jost, P., Hu, W., de Gouw, J., Koss, A., Cohen, R. C., Duffey, K. C., Romer,
600 P., Baumann, K., Edgerton, E., Takahama, S., Thornton, J. A., Lee, B. H., Lopez-Hilfiker, F. D., Mohr, C., Wennberg, P. O., Nguyen, T. B., Teng, A., Goldstein, A. H., Olson, K., and Fry, J. L.: Organic nitrate aerosol formation via NO$_3$ + biogenic volatile organic

compounds in the southeastern United States, Atmos. Chem. Phys., 15, 13377-13392, 10.5194/acp-15-13377-2015, 2015.

605 Barnes, I., Bastian, V., Becker, K. H., and Tong, Z.: KINETICS AND PRODUCTS OF THE REACTIONS OF NO3 WITH MONOALKENES, DIALKENES, AND MONOTERPENES, Journal of Physical Chemistry, 94, 2413-2419, 10.1021/j100369a041, 1990.

Berndt, T. and Boge, O.: Gas-phase reaction of NO3 radicals with isoprene: A kinetic and 610 mechanistic study, International Journal of Chemical Kinetics, 29, 755-765, 10.1002/(sici)1097-4601(1997)29:10<755::aid-kin4>3.0.co;2-l, 1997.

Berndt, T. and Böge, O.: Products and mechanism of the gas-phase reaction of NO_3 radicals with α-pinene, Journal of the Chemical Society, Faraday Transactions, 93, 3021-3027, 10.1039/A702364B, 1997.

615 Bohn, B.: Solar spectral actinic flux and photolysis frequency measurements in a deciduous forest, Journal of Geophysical Research: Atmospheres, 111, https://doi.org/10.1029/2005JD006902, 2006.

Brown, S. S. and Stutz, J.: Nighttime radical observations and chemistry, Chem. Soc. Rev., 41, 6405–6447, 2012.

620 Burkholder, J., Sander, S., Abbatt, J., Barker, J., Cappa, C., Crounse, J., Dibble, T., Huie, R., Kolb, C., and Kurylo, M.: Chemical kinetics and photochemical data for use in atmospheric studies; evaluation number 19, Jet Propulsion Laboratory, National Aeronautics and Space Administration, 2020.

Cantrell, C. and Michoud, V.: An Experiment to Study Atmospheric Oxidation Chemistry and 625 Physics of Mixed Anthropogenic–Biogenic Air Masses in the Greater Paris Area, Bulletin of the American Meteorological Society, 103, 599-603, https://doi.org/10.1175/BAMS-D-21-0115.1, 2022.

Claflin, M. S. and Ziemann, P. J.: Identification and Quantitation of Aerosol Products of the Reaction of β-Pinene with NO_3 Radicals and Implications for Gas- and Particle-Phase 630 Reaction Mechanisms, Journal of Physical Chemistry A, 122, 3640-3652, 10.1021/acs.jpca.8b00692, 2018.

Cox, R. A., Ammann, M., Crowley, J. N., Herrmann, H., Jenkin, M. E., McNeill, V. F., Mellouki, A., Troe, J., and Wallington, T. J.: Evaluated kinetic and photochemical data for atmospheric chemistry: Volume VII – Criegee intermediates, Atmos. Chem. Phys., 20, 635 13497-13519, 10.5194/acp-20-13497-2020, 2020.

Crowley, J.: ACROSS_MPIC_RambForest_O3_10min_L1 [dataset], https://doi.org/10.25326/707, 2023.

Crowley, J. N., Pouvesle, N., Phillips, G. J., Axinte, R., Fischer, H., Petäjä, T., Nölscher, A., Williams, J., Hens, K., Harder, H., Martinez-Harder, M., Novelli, A., Kubistin, D., Bohn, 640 B., and Lelieveld, J.: Insights into HO_x and RO_x chemistry in the boreal forest via measurement of peroxyacetic acid, peroxyacetic nitric anhydride (PAN) and hydrogen peroxide, Atmospheric Chemistry and Physics, 18, 13457-13479, 10.5194/acp-18-13457-2018, 2018.

Denjean, C.: ACROSS_CNRM_RambForest_MTO-1MIN_L2 [dataset], 645 https://doi.org/10.25326/437, 2023.

DeVault, M. P., Ziola, A. C., and Ziemann, P. J.: Products and Mechanisms of Secondary Organic Aerosol Formation from the NO_3 Radical-Initiated Oxidation of Cyclic and Acyclic Monoterpenes, ACS Earth and Space Chemistry, 6, 2076-2092, 10.1021/acsearthspacechem.2c00130, 2022.

650 Dewald, P. and Crowley, J. N.: ACROSS_MPIC_RambForest_ KNO3_10min_L2 [dataset], https://doi.org/10.25326/545, 2023.

Dewald, P., Seubert, T., Andersen, S. T., Türk, G. N. T. E., Schuladen, J., McGillen, M. R.,
Denjean, C., Etienne, J. C., Garrouste, O., Jamar, M., Harb, S., Cirtog, M., Michoud, V.,
Cazaunau, M., Bergé, A., Cantrell, C., Dusanter, S., Picquet-Varrault, B., Kukui, A., Xue,
655   C., Mellouki, A., Lelieveld, J., and Crowley, J. N.: NO_3 reactivity during a summer period
in a temperate forest below and above the canopy, Atmos. Chem. Phys., 24, 8983-8997,
10.5194/acp-24-8983-2024, 2024.

Draxler, R. R. and Rolph, G. D.: HYSPLIT (HYbrid Single-Particle Lagrangian Integrated
Trajectory)   Model   access   via   NOAA   ARL   READY   Website
660   (http://ready.arl.noaa.gov/HYSPLIT.php). NOAA Air Resources Laboratory, Silver
Spring, MD., 2011.

Eisele, F. L. and Tanner, D. J.: Ion-Assisted Tropospheric OH Measurements, Journal of
Geophysical Research-Atmospheres, 96, 9295-9308, 1991.

Fry, J. L., Draper, D. C., Barsanti, K. C., Smith, J. N., Ortega, J., Winkle, P. M., Lawler, M. J.,
665   Brown, S. S., Edwards, P. M., Cohen, R. C., and Lee, L.: Secondary Organic Aerosol
Formation and Organic Nitrate Yield from NO_3 Oxidation of Biogenic Hydrocarbons,
Environmental Science & Technology, 48, 11944-11953, 10.1021/es502204x, 2014.

Fry, J. L., Kiendler-Scharr, A., Rollins, A. W., Wooldridge, P. J., Brown, S. S., Fuchs, H.,
Dube, W., Mensah, A., dal Maso, M., Tillmann, R., Dorn, H. P., Brauers, T., and Cohen,
670   R. C.: Organic nitrate and secondary organic aerosol yield from NO_3 oxidation of beta-
pinene evaluated using a gas-phase kinetics/aerosol partitioning model, Atmospheric
Chemistry and Physics, 9, 1431-1449, 2009.

Fry, J. L., Kiendler-Scharr, A., Rollins, A. W., Brauers, T., Brown, S. S., Dorn, H. P., Dube,
W. P., Fuchs, H., Mensah, A., Rohrer, F., Tillmann, R., Wahner, A., Wooldridge, P. J., and
675   Cohen, R. C.: SOA from limonene: role of NO_3 in its generation and degradation,
Atmospheric Chemistry and Physics, 11, 3879-3894, 10.5194/acp-11-3879-2011, 2011.

Ge, Y., Solberg, S., Heal, M. R., Reimann, S., van Caspel, W., Hellack, B., Salameh, T., and
Simpson, D.: Evaluation of modelled versus observed non-methane volatile organic
compounds at European Monitoring and Evaluation Programme sites in Europe, Atmos.
680   Chem. Phys., 24, 7699-7729, 10.5194/acp-24-7699-2024, 2024.

Guenther, A. B., Jiang, X., Heald, C. L., Sakulyanontvittaya, T., Duhl, T., Emmons, L. K., and
Wang, X.: The Model of Emissions of Gases and Aerosols from Nature version 2.1
(MEGAN2.1): an extended and updated framework for modeling biogenic emissions,
Geoscientific Model Development, 5, 1471-1492, 10.5194/gmd-5-1471-2012, 2012.

685   Hallquist, M., Wangberg, I., Ljungstrom, E., Barnes, I., and Becker, K. H.: Aerosol and product
yields from NO_3 radical-initiated oxidation of selected monoterpenes, Environmental
Science & Technology, 33, 553-559, 10.1021/es980292s, 1999.

Hallquist, M., Wenger, J. C., Baltensperger, U., Rudich, Y., Simpson, D., Claeys, M.,
Dommen, J., Donahue, N. M., George, C., Goldstein, A. H., Hamilton, J. F., Herrmann, H.,
690   Hoffmann, T., Iinuma, Y., Jang, M., Jenkin, M. E., Jimenez, J. L., Kiendler-Scharr, A.,
Maenhaut, W., McFiggans, G., Mentel, T. F., Monod, A., Prevot, A. S. H., Seinfeld, J. H.,
Surratt, J. D., Szmigielski, R., and Wildt, J.: The formation, properties and impact of
secondary organic aerosol: current and emerging issues, Atmospheric Chemistry and
Physics, 9, 5155-5236, 10.5194/acp-9-5155-2009, 2009.

695   IUPAC Task Group on Atmospheric Chemical Kinetic Data Evaluation, (Ammann, M., Cox,
R.A., Crowley, J.N., Herrmann, H., Jenkin, M.E., McNeill, V.F., Mellouki, A., Rossi, M.
J., Troe, J. and Wallington, T. J.). Last access April. 2024: https://iupac.aeris-data.fr/, last

Kanakidou, M., Seinfeld, J., Pandis, S., Barnes, I., Dentener, F., Facchini, M., Dingenen, R.
V., Ervens, B., Nenes, A., and Nielsen, C.: Organic aerosol and global climate modelling:
700   a review, Atmospheric Chemistry and Physics, 5, 1053-1123, 10.5194/acp-5-1053-2005,
2005.

Kukui, A.: ACROSS_LPC2E_Rambforest_OH_L2 [dataset], https://doi.org/10.25326/510, 2023a.

Kukui, A.: ACROSS_LPC2E_Rambforest_RO2_L2 [dataset], https://doi.org/10.25326/509, 2023b.

Kukui, A., Ancellet, G., and Le Bras, G.: Chemical ionisation mass spectrometer for measurements of OH and Peroxy radical concentrations in moderately polluted atmospheres, Journal of Atmospheric Chemistry, 61, 133-154, 10.1007/s10874-009-9130-9, 2008.

Kukui, A., Chartier, M., Wang, J., Chen, H., Dusanter, S., Sauvage, S., Michoud, V., Locoge, N., Gros, V., Bourrianne, T., Sellegri, K., and Pichon, J. M.: Role of Criegee intermediates in the formation of sulfuric acid at a Mediterranean (Cape Corsica) site under influence of biogenic emissions, Atmos. Chem. Phys., 21, 13333-13351, 10.5194/acp-21-13333-2021, 2021.

Kwan, A. J., Chan, A. W. H., Ng, N. L., Kjaergaard, H. G., Seinfeld, J. H., and Wennberg, P. O.: Peroxy radical chemistry and OH radical production during the NO_3-initiated oxidation of isoprene, Atmospheric Chemistry and Physics, 12, 7499-7515, 10.5194/acp-12-7499-2012, 2012.

Liebmann, J., Karu, E., Sobanski, N., Schuladen, J., Ehn, M., Schallhart, S., Quéléver, L., Hellen, H., Hakola, H., Hoffmann, T., Williams, J., Fischer, H., Lelieveld, J., and Crowley, J. N.: Direct measurement of NO_3 radical reactivity in a boreal forest, Atmospheric Chemistry and Physics 2018, 3799-3815, 10.5194/acp-18-3799-2018, 2018a.

Liebmann, J., Sobanski, N., Schuladen, J., Karu, E., Hellén, H., Hakola, H., Zha, Q., Ehn, M., Riva, M., Heikkinen, L., Williams, J., Fischer, H., Lelieveld, J., and Crowley, J. N.: Alkyl nitrates in the boreal forest: formation via the NO_3-, OH- and O_3-induced oxidation of biogenic volatile organic compounds and ambient lifetimes, Atmos. Chem. Phys., 19, 10391-10403, 10.5194/acp-19-10391-2019, 2019.

Liebmann, J. M., Muller, J. B. A., Kubistin, D., Claude, A., Holla, R., Plass-Dülmer, C., Lelieveld, J., and Crowley, J. N.: Direct measurements of NO_3 reactivity in and above the boundary layer of a mountaintop site: identification of reactive trace gases and comparison with OH reactivity, Atmospheric Chemistry and Physics, 18, 12045-12059, 10.5194/acp-18-12045-2018, 2018b.

Lightfoot, P. D., Cox, R. A., Crowley, J. N., Destriau, M., Hayman, G. D., Jenkin, M. E., Moortgat, G. K., and Zabel, F.: Organic peroxy radicals - kinetics, spectroscopy and tropospheric chemistry, Atmospheric Environment, Part A: General Topics, 26, 1805-1961, 1992.

Mellouki, A., Ammann, M., Cox, R. A., Crowley, J. N., Herrmann, H., Jenkin, M. E., McNeill, V. F., Troe, J., and Wallington, T. J.: Evaluated kinetic and photochemical data for atmospheric chemistry: volume VIII – gas-phase reactions of organic species with four, or more, carbon atoms., Atmos. Chem. Phys., 21, 4797-4808, 10.5194/acp-21-4797-2021, 2021.

Meusel, H., Kuhn, U., Reiffs, A., Mallik, C., Harder, H., Martinez, M., Schuladen, J., Bohn, B., Parchatka, U., Crowley, J. N., Fischer, H., Tomsche, L., Novelli, A., Hoffmann, T., Janssen, R. H. H., Hartogensis, O., Pikridas, M., Vrekoussis, M., Bourtsoukidis, E., Weber, B., Lelieveld, J., Williams, J., Pöschl, U., Cheng, Y., and Su, H.: Daytime formation of nitrous acid at a coastal remote site in Cyprus indicating a common ground source of atmospheric HONO and NO, Atmospheric Chemistry and Physics, 16, 14475-14493, 10.5194/acp-16-14475-2016, 2016.

Michoud, V., Bouzidi, H., Formenti, P., Bauville, A., Cazaunau, M., Alage, S., Cirtog, M., De Haan, D., and Rafla, M.:

ACROSS_2022_RambForest_LISA_PTRMS_VOCs_Belowcanopy_10min_20220617 - 20220723 [dataset], https://doi.org/10.25326/685, 2024.

Ng, N. L., Brown, S. S., Archibald, A. T., Atlas, E., Cohen, R. C., Crowley, J. N., Day, D. A., Donahue, N. M., Fry, J. L., Fuchs, H., Griffin, R. J., Guzman, M. I., Herrmann, H., Hodzic, A., Iinuma, Y., Jimenez, J. L., Kiendler-Scharr, A., Lee, B. H., Luecken, D. J., Mao, J., McLaren, R., Mutzel, A., Osthoff, H. D., Ouyang, B., Picquet-Varrault, B., Platt, U., Pye, H. O. T., Rudich, Y., Schwantes, R. H., Shiraiwa, M., Stutz, J., Thornton, J. A., Tilgner, A., Williams, B. J., and Zaveri, R. A.: Nitrate radicals and biogenic volatile organic compounds: oxidation, mechanisms, and organic aerosol, Atmospheric Chemistry and Physics, 17, 2103-2162, 10.5194/acp-17-2103-2017, 2017.

Nozière, B., Barnes, I., and Becker, K.-H.: Product study and mechanisms of the reactions of α-pinene and of pinonaldehyde with OH radicals, Journal of Geophysical Research: Atmospheres, 104, 23645-23656, https://doi.org/10.1029/1999JD900778, 1999.

Perring, A. E., Pusede, S. E., and Cohen, R. C.: An observational perspective on the atmospheric impacts of alkyl and multifunctional nitrates on ozone and secondary organic aerosol, Chemical Reviews, 113, 5848-5870, doi:10.1021/cr300520x, 2013.

Perring, A. E., Wisthaler, A., Graus, M., Wooldridge, P. J., Lockwood, A. L., Mielke, L. H., Shepson, P. B., Hansel, A., and Cohen, R. C.: A product study of the isoprene+NO$_3$ reaction, Atmospheric Chemistry and Physics, 9, 4945-4956, 2009.

Rindelaub, J. D., McAvey, K. M., and Shepson, P. B.: The photochemical production of organic nitrates from alpha-pinene and loss via acid-dependent particle phase hydrolysis, Atmospheric Environment, 100, 193-201, 10.1016/j.atmosenv.2014.10.010, 2015.

Rollins, A. W., Kiendler-Scharr, A., Fry, J. L., Brauers, T., Brown, S. S., Dorn, H. P., Dubé, W. P., Fuchs, H., Mensah, A., Mentel, T. F., Rohrer, F., Tillmann, R., Wegener, R., Wooldridge, P. J., and Cohen, R. C.: Isoprene oxidation by nitrate radical: alkyl nitrate and secondary organic aerosol yields, Atmospheric Chemistry and Physics, 9, 6685-6703, 10.5194/acp-9-6685-2009, 2009.

Sander, R., Baumgaertner, A., Cabrera-Perez, D., Frank, F., Gromov, S., Grooss, J. U., Harder, H., Huijnen, V., Jockel, P., Karydis, V. A., Niemeyer, K. E., Pozzer, A., Hella, R. B., Schultz, M. G., Taraborrelli, D., and Tauer, S.: The community atmospheric chemistry box model CAABA/MECCA-4.0, Geoscientific Model Development, 12, 1365-1385, 10.5194/gmd-12-1365-2019, 2019.

Schwantes, R. H., Teng, A. P., Nguyen, T. B., Coggon, M. M., Crounse, J. D., St Clair, J. M., Zhang, X., Schilling, K. A., Seinfeld, J. H., and Wennberg, P. O.: Isoprene NO$_3$ Oxidation Products from the RO$_2$ + HO$_2$ Pathway, Journal of Physical Chemistry A, 119, 10158-10171, 10.1021/acs.jpca.5b06355, 2015.

Shepson, P. B., Bottenheim, J. W., Hastie, D. R., and Venkatram, A.: Determination of the relative ozone and PAN deposition velocities at night, Geophysical Research Letters, 19, 1121-1124, 10.1029/92gl01118, 1992.

Shiraiwa, M., Ueda, K., Pozzer, A., Lammel, G., Kampf, C. J., Fushimi, A., Enami, S., Arangio, A. M., Fröhlich-Nowoisky, J., Fujitani, Y., Furuyama, A., Lakey, P. S. J., Lelieveld, J., Lucas, K., Morino, Y., Pöschl, U., Takahama, S., Takami, A., Tong, H., Weber, B., Yoshino, A., and Sato, K.: Aerosol Health Effects from Molecular to Global Scales, Environmental Science & Technology, 51, 13545-13567, 10.1021/acs.est.7b04417, 2017.

Sobanski, N., Schuladen, J., Schuster, G., Lelieveld, J., and Crowley, J. N.: A five-channel cavity ring-down spectrometer for the detection of NO$_2$, NO$_3$, N$_2$O$_5$, total peroxy nitrates and total alkyl nitrates, Atmospheric Measurement Techniques, 9, 5103-5118, 10.5194/amt-9-5103-2016, 2016.

800   Spittler, M., Barnes, I., Bejan, I., Brockmann, K. J., Benter, T., and Wirtz, K.: Reactions of NO$_3$ radicals with limonene and alpha-pinene: Product and SOA formation, Atmospheric Environment, 40, S116-S127, 10.1016/j.atmosenv.2005.09.093, 2006.

Thieser, J., Schuster, G., Phillips, G. J., Reiffs, A., Parchatka, U., Pöhler, D., Lelieveld, J., and Crowley, J. N.: A two-channel, thermal dissociation cavity-ringdown spectrometer for the
805   detection of ambient NO$_2$, RO$_2$NO$_2$ and RONO$_2$, Atmos. Meas. Tech., 9, 553-576, 10.5194/amt-9-553-2016, 2016.

Wängberg, I., Barnes, I., and Becker, K. H.: Product and Mechanistic Study of the Reaction of NO3 Radicals with#±-Pinene, Environmental Science & Technology, 31, 2130-2135, 1997.

810   Wennberg, P. O., Bates, K. H., Crounse, J. D., Dodson, L. G., McVay, R. C., Mertens, L. A., Nguyen, T. B., Praske, E., Schwantes, R. H., Smarte, M. D., St Clair, J. M., Teng, A. P., Zhang, X., and Seinfeld, J. H.: Gas-Phase Reactions of Isoprene and Its Major Oxidation Products, Chemical Reviews, 118, 3337-3390, 10.1021/acs.chemrev.7b00439, 2018.

Wolfe, G. M., Thornton, J. A., Bouvier-Brown, N. C., Goldstein, A. H., Park, J. H., McKay,
815   M., Matross, D. M., Mao, J., Brune, W. H., LaFranchi, B. W., Browne, E. C., Min, K. E., Wooldridge, P. J., Cohen, R. C., Crounse, J. D., Faloona, I. C., Gilman, J. B., Kuster, W. C., de Gouw, J. A., Huisman, A., and Keutsch, F. N.: The Chemistry of Atmosphere-Forest Exchange (CAFE) Model – Part 2: Application to BEARPEX-2007 observations, Atmos. Chem. Phys., 11, 1269-1294, 10.5194/acp-11-1269-2011, 2011.

820   Xue, C., Mcgillen, M., and Mellouki, A.: ACROSS_ICARE_RambForest_NO_L2 [dataset], https://doi.org/10.25326/512, 2023.

Zheng, W., Flocke, F. M., Tyndall, G. S., Swanson, A., Orlando, J. J., Roberts, J. M., Huey, L. G., and Tanner, D. J.: Characterization of a thermal decomposition chemical ionization mass spectrometer for the measurement of peroxy acyl nitrates (PANs) in the atmosphere,
825   Atmospheric Chemistry and Physics, 11, 6529-6547, 2011.

827 **11 Figures:**
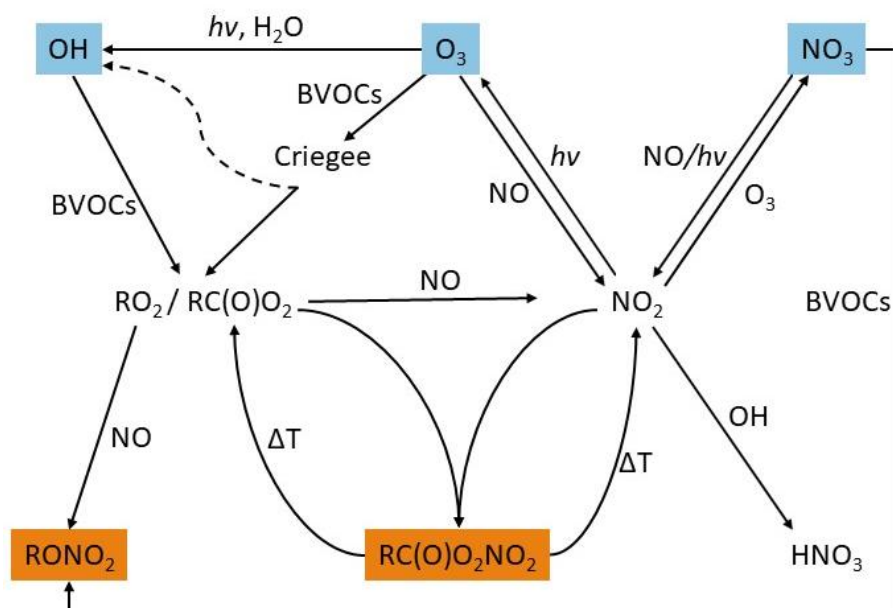
828

829 Figure 1: Schematic diagram showing the formation of PANs (RC(O)$O_2$$NO_2$) and ANs (RONO$_2$)
830 from the oxidation of VOCs by OH, O_3, and NO_3. Reactions of RO$_2$ not relevant to the formation
831 of RC(O)$O_2$$NO_2$ and RONO$_2$ have been left out. Note that the scheme does not attempt to capture
832 all formation routes of the primary oxidants, especially those of the OH-radical, which may
833 additionally be formed in e.g. reactions of HO$_2$ with OH and photolysis of HONO.

834
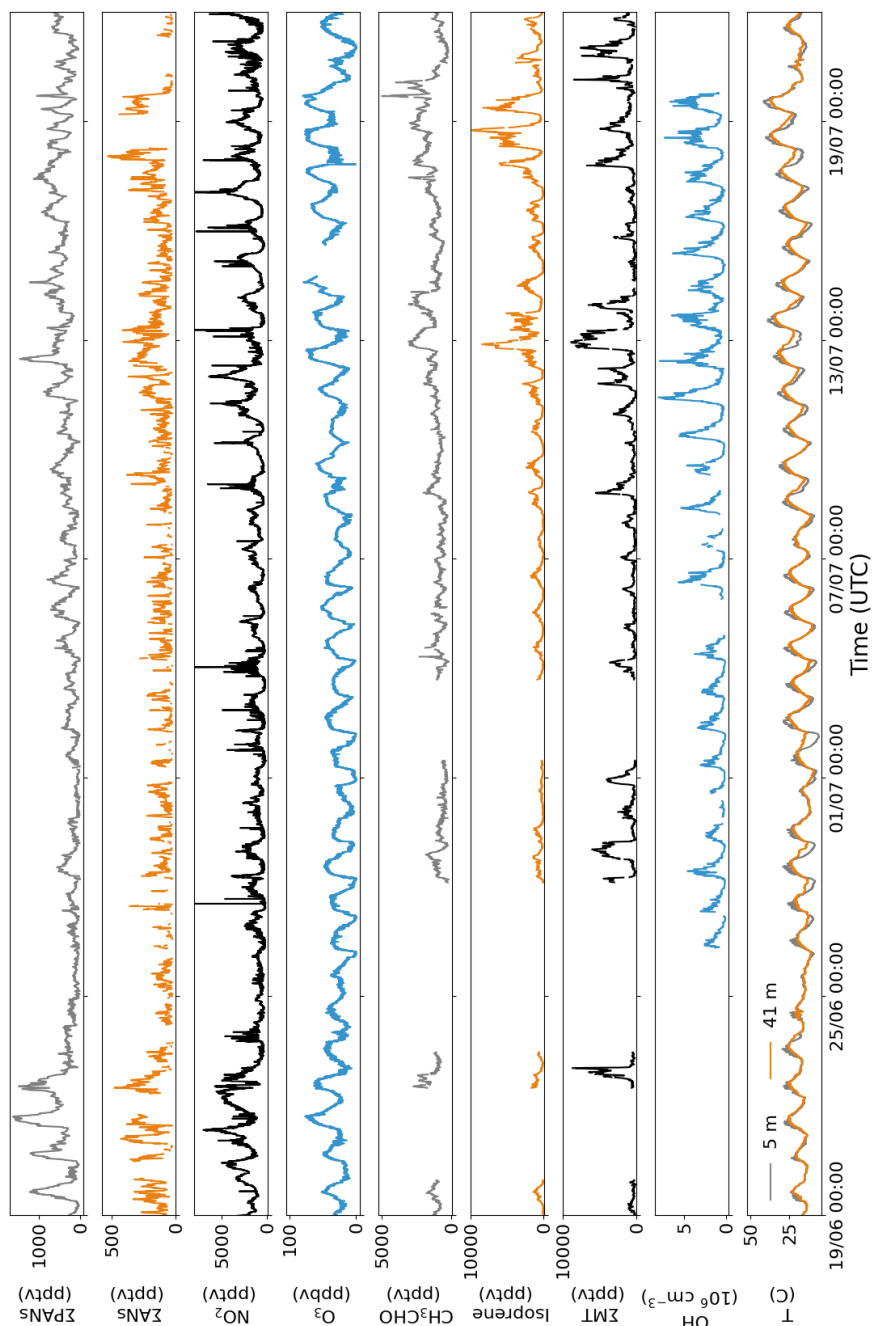
Figure 2: Time series of 10-minute averages of ∑PANs, ∑ANs, acetaldehyde, isoprene, and sum
of monoterpenes (∑MT), 12-minute averages of OH radicals, and 1-minute averages of NO_2, O_3,
and temperature at 5 and 41 m during the ACROSS campaign.

838
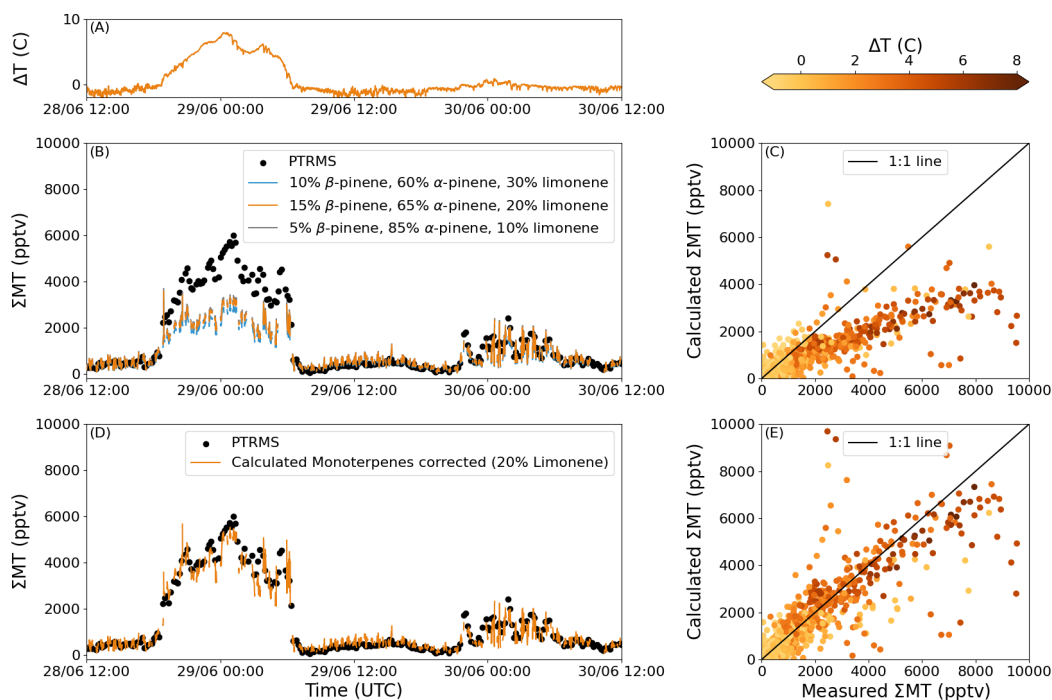
Figure 3: NO₃-reactivity based estimation of monoterpene mixtures during ACROSS. Panel A
shows the difference in temperature between 41 m and 5 m ($\Delta T = T_{41m}-T_{5m}$) for 48 hours during
ACROSS. Panel B shows the measured sum of monoterpenes ($\sum MT$) and that calculated using eq.
(1) with three different monoterpene mixtures. Panel C plots calculated against measured $\sum MT$
for the scenario with 20% limonene coloured by ΔT. Panel D shows the scenario with 20%
limonene from panel C using a mixture of 57% β-pinene and 43% α-pinene when $\Delta T>1°C$ and
panel E shows the scatter plot after performing the correction for temperature inversions.

846

847

848
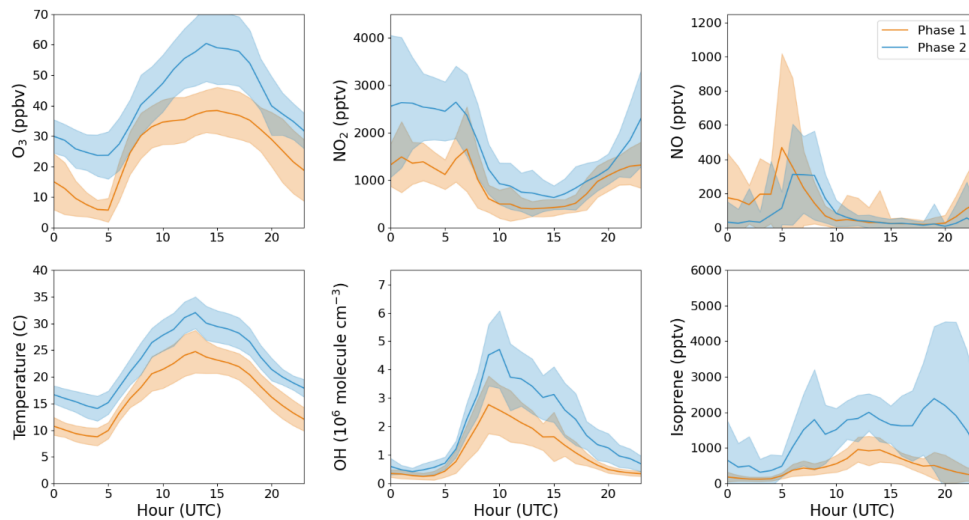
Figure 4: Diel profiles of O_3, NO_2, NO, temperature, OH, and isoprene for the two phases used to analyse organic nitrates during the ACROSS campaign; phase 1 from June 28th 2022 to July 7th 2022 and phase 2 from July 8th 2022 to July 20th 2022. The shaded area is ±1σ.
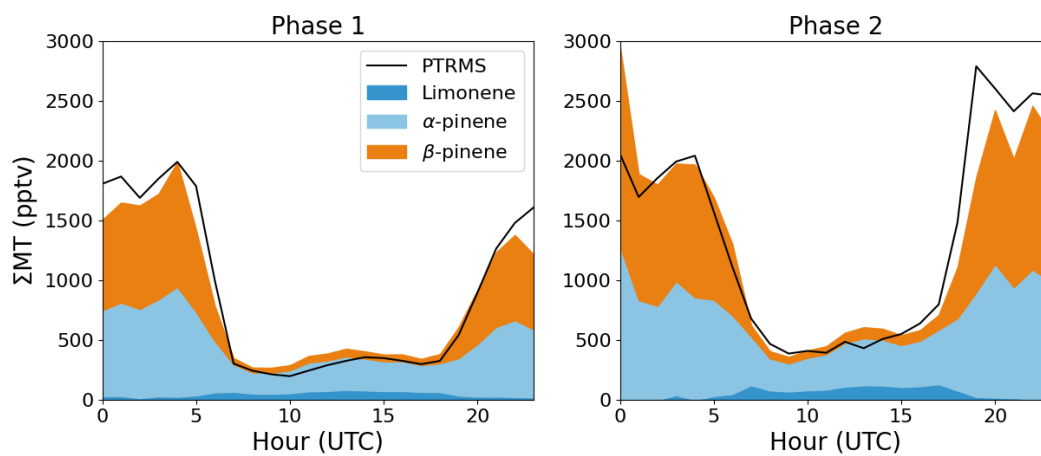
Figure 5: Average diel profiles of the PTRMS measurements of the sum of monoterpenes (black) and the calculated, average mixture of limonene (dark blue), α-pinene (light blue), and β-pinene (orange) for the scenario with 20% limonene.
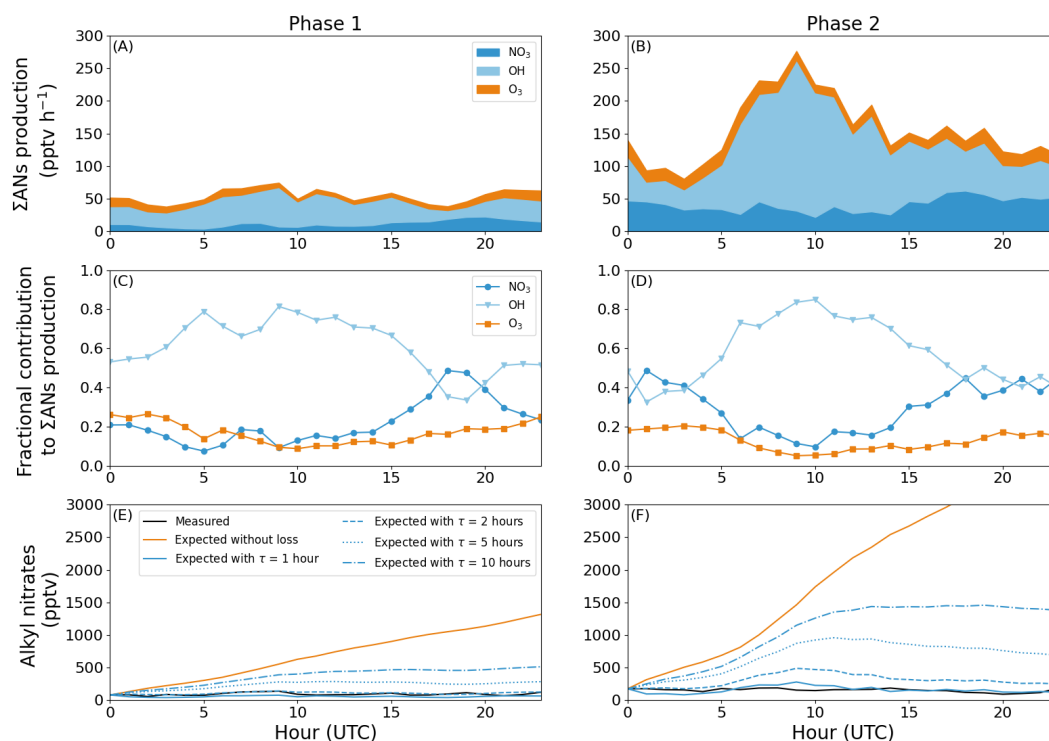
Figure 6: Panel A and B show the diel profiles of the $\sum$ANs production rates from NO$_3$-, OH-, and O$_3$-initiated oxidation of a monoterpene mixture consisting of 20% limonene, 15% β-pinene, and 65% α-pinene for phase 1 and 2, respectively. The fractional contribution to the $\sum$ANs for each oxidant is plotted in panel C and D. Panel E and F show the average diel profile across the two phases for the measured alkyl nitrates (black), expected alkyl nitrates with (blue) and without (orange) any losses, where the different blue lines were calculated using different effective lifetimes of the alkyl nitrates.

864
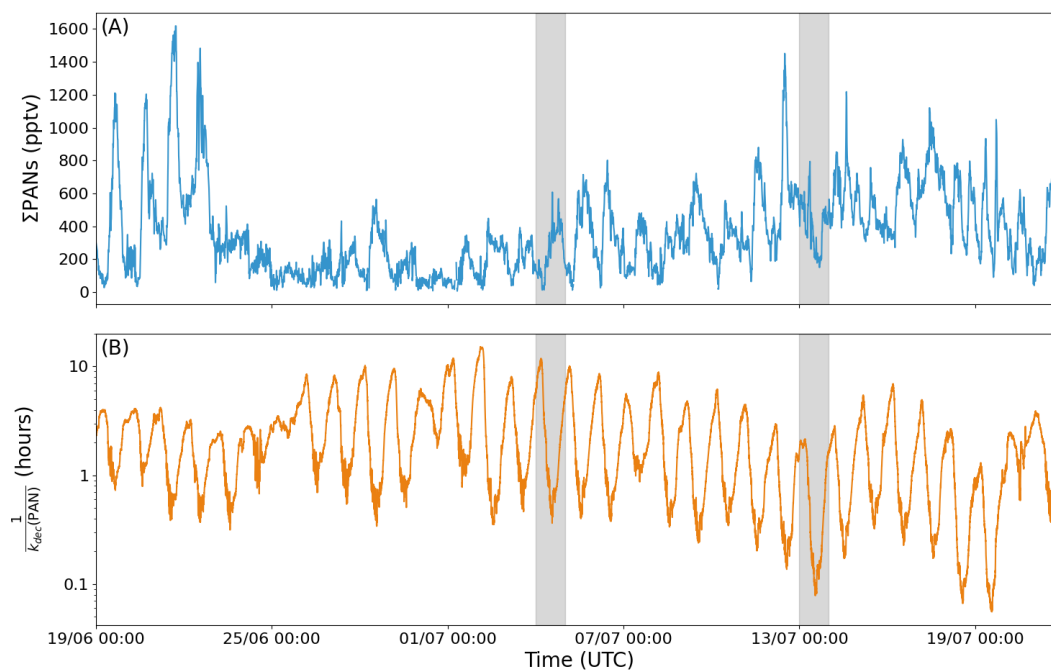
Figure 7: Time series of ∑PANs (A) and the thermal lifetime of PAN (B) during ACROSS, where
k_{dec} is the temperature dependent rate coefficient for the thermal decomposition of PAN using the
expression preferred by the IUPAC panel (Iupac, 2024). Days marked in grey are used for analysis
in Figure 8.
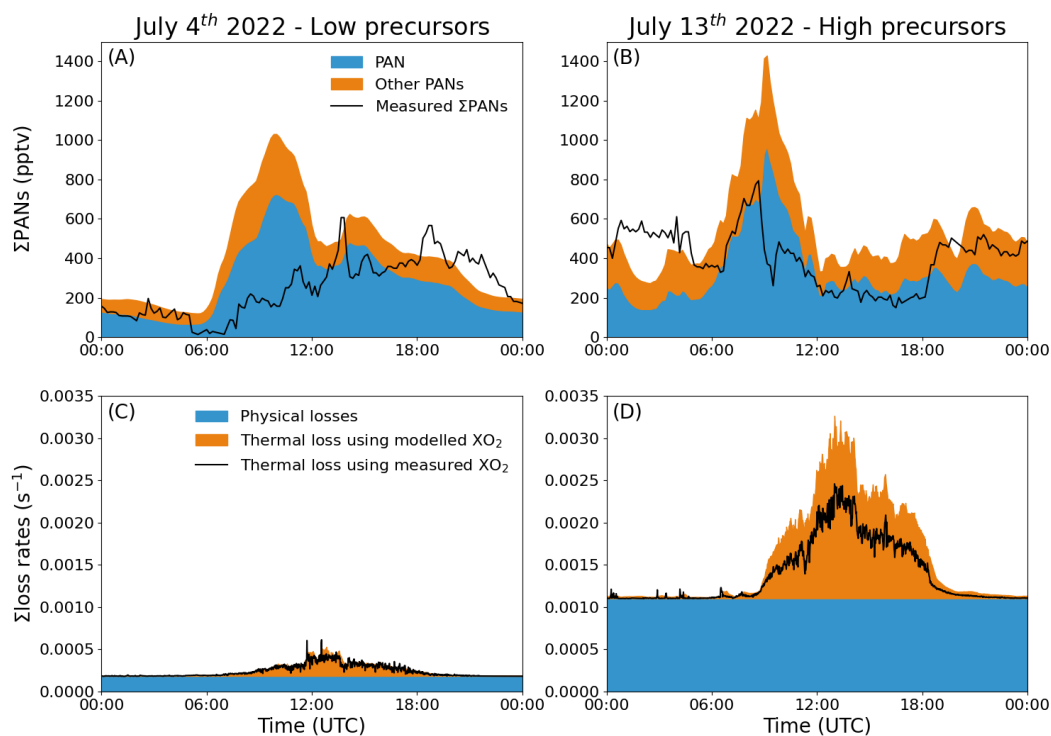
Figure 8: The measured and modelled when optimizing for nighttime agreement ∑PANs is plotted for two individual days; one with low precursors (A) and one with high precursors (B). The optimised physical loss for each day is shown in panel C and D together with the thermal decomposition when taking recombination into account using both the measured and modelled mixing ratio of XO_2.

12 Tables:

Table 1: Rate coefficients and relevant yields for the calculation of $\sum P_{ANs}$

VOC	$k(NO_3)$ at 298 K (cm^3 molecules^{-1} s^{-1})	α^{NO_3}	$k(OH)$ at 298 K (cm^3 molecules^{-1} s^{-1})	α^{RO_2}	$k(O_3)$ at 298 K (cm^3 molecules^{-1} s^{-1})	α^{O_3} [i]
α-pinene	6.2×10^{-12} [a]	0.18 [b]	5.3×10^{-11} [a]	0.22 [f]	9.6×10^{-17} [a]	0.80 [a]
β-pinene	2.5×10^{-12} [a]	0.49 [c]	7.6×10^{-11} [a]	0.24 [g]	1.9×10^{-17} [a]	0.30 [a]
d-limonene	1.2×10^{-11} [a]	0.50 [d]	1.7×10^{-10} [a]	0.23 [g]	2.2×10^{-16} [a]	0.66 [a]
Isoprene	6.5×10^{-13} [a]	0.77 [e]	1.0×10^{-10} [a]	0.13 [h]	1.28×10^{-17} [a]	0.26 [a]

α^{NO_3}: Yield of ANs from NO_3+BVOC in air.

α^{RO_2}: Yield of ANs from RO_2+NO for the specific BVOC when the RO_2 is formed from BVOC+OH.

α^{O_3}: Yield of RO_2 from the ozonolysis of BVOC in air.

[a] Rate coefficients and yields recommended by IUPAC(Iupac, 2024; Mellouki et al., 2021; Cox et al., 2020).

[b] Average of Wängberg et al. (1997), Berndt and Böge (1997), Hallquist et al. (1999), Spittler et al. (2006), Fry et al. (2014), and Devault et al. (2022).

[c] Average of Hallquist et al. (1999), Fry et al. (2009), Fry et al. (2014),Claflin and Ziemann (2018), and Devault et al. (2022).

[d] Average of Hallquist et al. (1999), Spittler et al. (2006), Fry et al. (2011), Fry et al. (2014), and Devault et al. (2022).

[e] Average of Barnes et al. (1990), Berndt and Boge (1997), Perring et al. (2009), Kwan et al. (2012), Rollins et al. (2009), and Schwantes et al. (2015).

[f] Average of the yields given by Nozière et al. (1999) and Rindelaub et al. (2015).

[g] Perring et al. (2013).

[h] Recommended by Wennberg et al. (2018) based on multiple studies.

[i] Set equal to the OH yield of the ozonolysis since a RO_2 is formed with each OH.

Table 2: Overview of the thermal, physical and total loss frequencies (and lifetimes) of ANs and PANs needed to explain the measured ANs and PANs during ACROSS.

		Phase 1 (Low photochemical activity)		Phase 2 (High photochemical activity)	
		Day	Night	Day	Night
ANs	Thermal loss frequency (s^{-1})[a]	-	-	-	-
	Physical loss frequency (10^{-4} s^{-1})	1.7 ± 0.3	1.7 ± 0.4	3.3 ± 0.8	2.5 ± 0.9
	Total loss frequency (10^{-4} s^{-1})	1.7 ± 0.3	1.7 ± 0.4	3.3 ± 0.8	2.5 ± 0.9
	Total lifetime (h)	1.7 ± 0.2	1.7 ± 0.5	0.9 ± 0.2	1.3 ± 0.5
PANs	Thermal loss frequency (10^{-4} s^{-1})[a]	1.2 ± 0.8	0.1 ± 0.1	8.8 ± 5.9	0.8 ± 1.3
	Physical loss frequency (10^{-4} s^{-1})	5.5	1.8	26	11
	Total loss frequency (10^{-4} s^{-1})	6.7 ± 0.8	1.9 ± 0.1	34.8 ± 5.9	11.8 ± 1.3
	Total lifetime (h)	0.42 ± 0.05	1.5 ± 0.1	0.08 ± 0.01	0.24 ± 0.02

[a] The thermal loss frequency has been corrected for the fractional recombination of $CH_3C(O)O_2$ with NO_2.

Day is defined as 06:00-18:00 UTC (08:00-20:00 LT). Night is defined as 18:00-06:00 UTC (20:00-08:00 LT).

All values except the modelled physical loss frequencies for PANs are given as the mean ± 1σ. The ANs are based on hourly averages for each phase and the PANs are based on modelled loss frequencies for one day during each phase.